NIAC Final Report

Steering of Solar Sails Using Optical Lift Force

Grover A. Swartzlander, Jr.
Rochester Institute of Technology

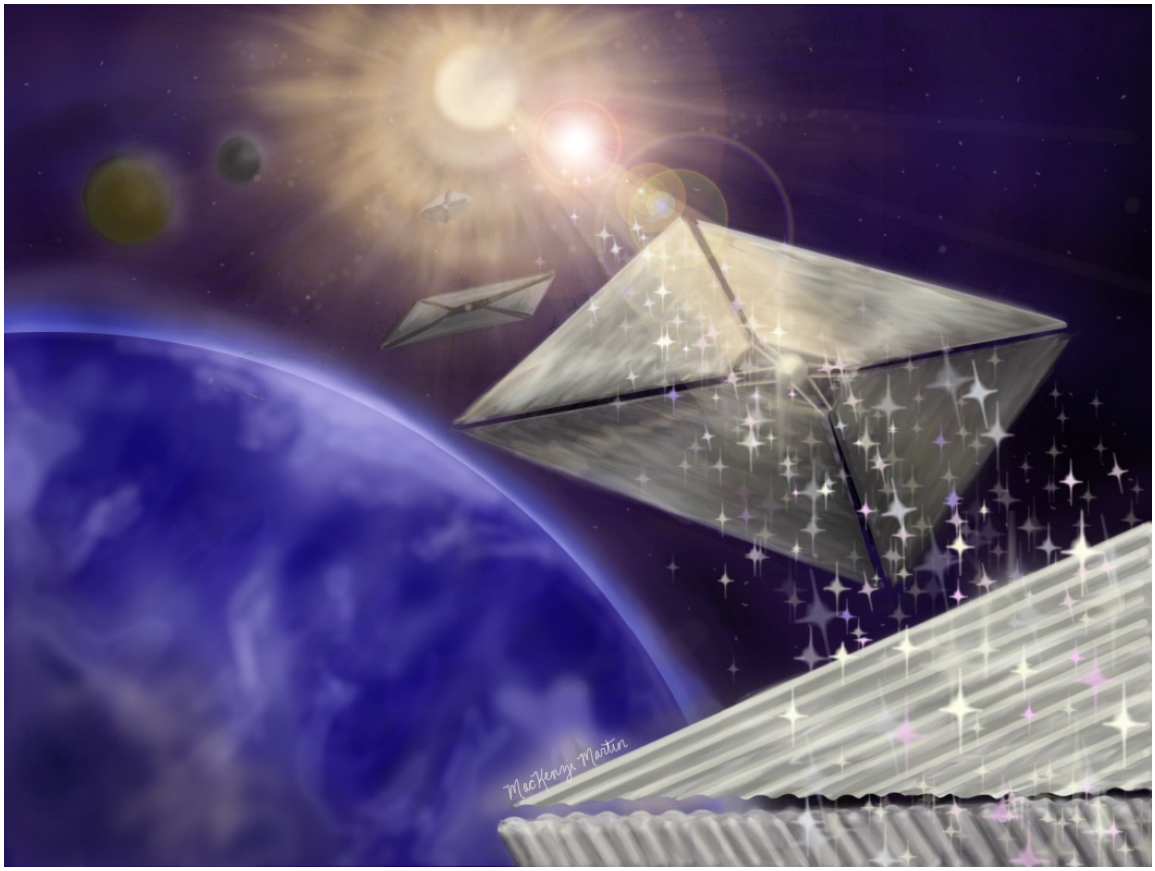

Acknowledgements

Alexandra Artusio-Glimpse, Rochester Institute of Technology, Rochester, NY
Alan Raisanen, Rochester Institute of Technology, Rochester, NY
Stephen Simpson, Univ. Bristol, UK
Charles (Les) Johnson, NASA Marshall Space Flight Center, Huntsville, AL
Andrew Heaton, NASA Marshall Space Flight Center, Huntsville, AL
Catherine Faye, NASA Langley, Langley, VA
John Dankanich, NASA Glenn, Cleveland, OH
Amy Davis, NeXolve Corp., Huntsville, AL

SUMMARY

Optical wing structures were theoretically and numerically analyzed, and prototype arrays of wings called optical flying carpets were fabricated with solar sail material clear polyimide (CP1). This material was developed at NASA Langley to better withstand damaging ultraviolet radiation found in outer space. Various optical wing sizes and shapes were analyzed to develop design strategies for thrust and torque applications. The developed ray-tracing model has undergone continual advancement, and stands as an effective tool for modeling most types of solar sails. To our understanding, such a model does not exist elsewhere. The distributed forces and torques have been reduced to a simple theoretical whereby the fundamental mechanics may be understood in terms of the numerically determined center of pressure offset from the center of mass. This description applies to any type of solar sail, affording our ray-tracing model a general utility. This research has established a foundation for understanding the force and torque afforded by optical wings. The study began by considering transparent wings and ended by considering wings having a reflecting face. The latter was found to afford the advantages of high thrust and both intrinsic and extrinsic torque. Our discovery of the intrinsic torque on optical wings (meaning that a moment arm is not required) has no analogy for a flat reflective solar sail, and therefore provides an extra degree of control that may be useful for sailcraft attitude and navigation purposes.

THEORETICAL

Radiation pressure is exerted on an object owing to the absorption or redirection of electromagnetic momentum. Redirected momentum is attributed to refraction, reflection, or re-emission of light. Assuming low loss, absorption and re-emission may be ignored. Numerical methods are required to determine the force and torque exerted on a refractive and/or reflective body of arbitrary shape. We have used both ray-tracing and wave-optics models to explore how basic elements, namely long cambered rods, are pushed and rotated when uniformly illuminated by a beam of light. Following examples found in aeronautics, we have developed the theory of radiation pressure in terms of an applied center of pressure, thereby reducing a complicated system to an elegant formalism.

Flat Reflecting Sail

It is instructive to first consider the force and torque exerted on a uniformly illuminated flat reflective sail, as illustrated in Fig. 1. Light directed along the x-axis ($\phi = \pi/2$, $\theta = 0$) The is incident on the surface at angles θ and ϕ, resulting in a force that is normal to the surface:

$$\bar{\mathrm{f}} = 2(IA/c)(\hat{n}\cdot\,\hat{x})^2\hat{n} \tag{1}$$

where $\hat{n} = \sin\phi\cos\theta\hat{x} + \hat{y}\sin\phi\sin\theta\hat{y} + \cos\phi\hat{z}$ is the unit normal vector of the surface of area A. The solar irradiance is given by $I = L/4\pi r^2$, where $L = 385 \times x10^{24}$ [J/s] is the broad-spectrum solar luminous flux and r is the distance from the sun. At $r = 1$ [AU] = $150 \times \mathrm{x}10^{9}$ [m] the maximum value of solar pressure is $P_{\max} = 2I/c = 9.12 \times 10^{-6}$ [N/m^2]. This pressure is roughly four orders of magnitude greater than the solar wind pressure [McInnes 1999, p. 54]. For a sailcraft of total mass *m* and sail area *A*, the acceleration is given by $a = P/\sigma$, where $\sigma = m/A$ is the areal density. At 1 [AU] from the sun, the gravitational acceleration of the sun is $a_{sun} = GM/r^2 = 5.9$ [mm/s^2]. The sailcraft may experience an equal and opposite acceleration at an areal density $\sigma_0 = P/a_{sun} = 1.54$ [g/m^2]. Note that this value is independent of the distance from the sun, since both forces decrease inversely with

the squared distance. From this gravitational point of view, the sailcraft acceleration may be expressed in terms of the "lightness" number $\beta = \sigma_0 / \sigma$, mass of the sun M_S, and gravitational const, G:

$$\vec{a} = (\beta G M_S / r^2)(\hat{n} \cdot \hat{x})^2 \hat{n} \tag{2}$$

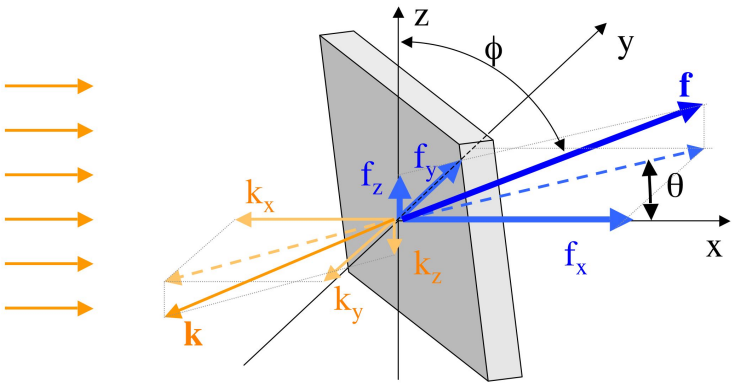

Figure 1. Light incident in the x-direction on a perfectly reflective surface. Reflected light produces a radiation pressure force in the direction **f**, normal to the surface.

Radiation Pressure on an Arbitrary Body

The net radiation pressure force on an arbitrary body may be expressed in terms of an efficiency vector, $\vec{Q}$ whose magnitude is $Q = 2$ for a perfect sun-facing sail ($\phi = \pi/2$, $\theta = 0$):

$$\vec{f} = (IA / c)\vec{Q} \tag{3}$$

Based on the conservation of momentum, we have determined that the optimal theoretical values of the longitudinal and transverse components of efficiency are given (assuming $\phi = \pi/2$) by

$$Q_{x,\text{opt}} = 1 - \cos(2\theta), \quad Q_{y,\text{opt}} = \sin(2\theta) \tag{4}$$

Figure 2 (left) shows these values plotted as a red circle, with the flat solar sail values plotted as a black ellipse. We note that our calculated optimal value predicts a transverse efficiency as large as $Q_y = 1$, whereas the flat sail can only achieve $Q_y = 0.77$. The latter occurs when $\theta \sim 35°$, $\phi = \pi/2$.

The x-component of force may be called the "forward scattering" or "thrust" component, whereas the y-component may be called the "lift" component. The word "lift" refers to a force in a direction perpendicular to the flow of incident light.

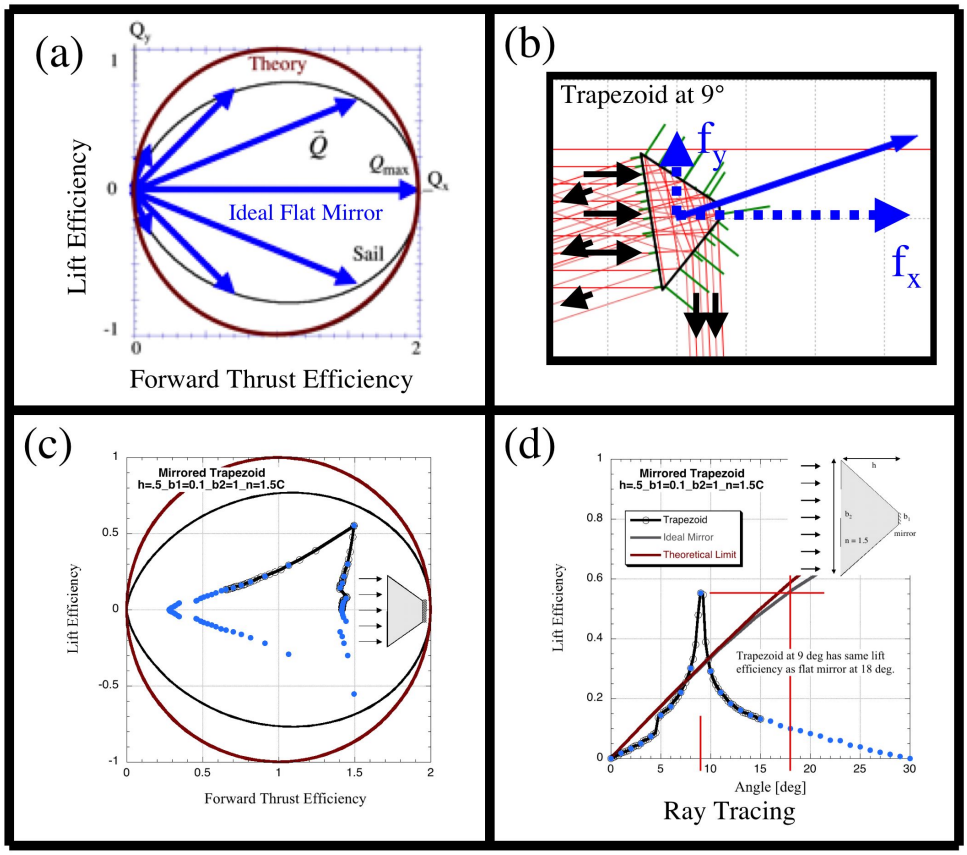

Figure 2. (a) Efficiency of radiation pressure force of a flat reflecting sail (blue arrows) does not achieve the theoretical limit (dark red circle) allowed by the conservation of momentum. (b) Ray tracing for a trapezoid, shown at an angle of attack of 9°. (c) Same at (a) but with the parametric efficiency curve for a trapezoid. (d) Lift efficiency as a function of angle of attack, showing lift values great than a flat reflector at 9°.

A flat reflective sail cannot reach the theoretical maximum lift efficiency owing to the factor cosθ that is attributed to the angle dependences of the sail cross-sectional area. That is, a tilted sail collects less light to reflect. This is depicted in Fig. 2(a). A solution to this problem would be to design the sail cross-section to be nearly sun-facing, while simultaneously deflecting the light perpendicular to the sun-line. This may allow the sail to perform at the physical limit (red line in Fig. 2 (a)). We considered various means to enhance the lift efficiency using single or arrayed optical wings. Although we found examples, such as the trapezoid in Fig. 2(b), where the lift force at a given angle of attack exceeded the lift force of a flat reflective sail at the same angle, we did not find examples exceeding the force vector ellipse, shown by the black line in Fig. 2 (a). For example, when a funnel-like trapezoid have a reflective smaller rear surface is placed in the beam, we predict a constant forward scattering force for angles of attack over the range ±9° (see Fig. 2(c)) where the forward thrust efficiency is ~1.5 while the lift efficiency varies from ±50%). What is more, this wing design provides more lift force than a comparable flat reflective sail, even though the trapezoid mirror surface is only 10% of that of a flat mirror. This means that the funnel-wing could (1) more readily provide maneuvering action than a flat mirrored surface, and (2) vary the lift force without affecting the forward scattering force. As this example illustrates, the shape of the wing may be tailored to suit a particular application over a range of orientation angles. As we explored only a narrow region of parameter space, e.g., varying the wing cross-sectional shape (see Fig. 3) and refractive index, the results in Fig. 2 suggest that greater optimization of large lift efficiencies is possible.

Controlling the lift force is an import component in the navigation of a sailcraft. For example, orbit-raising or orbit-lowering can be achieved by accelerating or decelerating the sailcraft along an orbital trajectory. Precise maneuvering of the craft may also be desired – for example, in a mission to encounter space debris, or to maintain a formation relative to other crafts. In many cases, it may be disadvantageous to tilt the entire sailcraft. Various mechanisms, such as motor-driven tip vanes, and actuated ballast mass have been proposed to achieve fine-scale attitude control. Here we have explored the feasibility of using optical wings to lift and torque a sailcraft.

An optical wing is an analog to an airfoil. It is a long structure having a cambered cross-section. Examples of optical wings are shown in Fig. 3. In this study we assume the wings have a length greater than other dimensions, therefore reducing the problem to two dimensions. We also assume they are composed of a non-absorbing homogenous, isotropic dielectric material of refractive index *n*. In some cases we allow for a reflective coating on one of the facets.

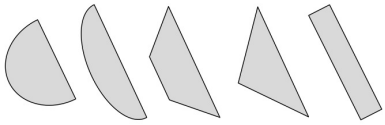

Figure 3. Example of optical wing cross-sections. Bodies may be refractive with optional reflective coatings over selected facets.

The radiation pressure force and torque on such bodies will depend on the orientation or "angle of attack" relative to the incident beam of light. Force and torque plots are discussed in the Numerical section. Here we discuss the mechanics of the wing for an arbitrary value of force and torque. In general the "center of pressure" (cp) will be offset from the center of mass (cm), causing the body to rotate. If the net force and torque is known at a given angle of attack, the center of pressure $\vec{r}_{cp}$ is found by satisfying the expressions:

$$\vec{r}_{cp} \times \vec{\mathrm{f}} = \vec{T}, \quad \vec{r}_{cp} \cdot \vec{\mathrm{f}} = 0 \tag{5}$$

Figure 4 depicts the centers of mass and pressure for a uniformly illuminated glass rod have a semicircular cross-section. In this diagram, the wing has a scattering force (in the direction of the incident rays), an upward lift force, and a torque that rotates the body clockwise. As shown in the right hand side of Fig. 4, the wing can assume different trajectories when the initial orientation is not in a rotationally stable equilibrium state.

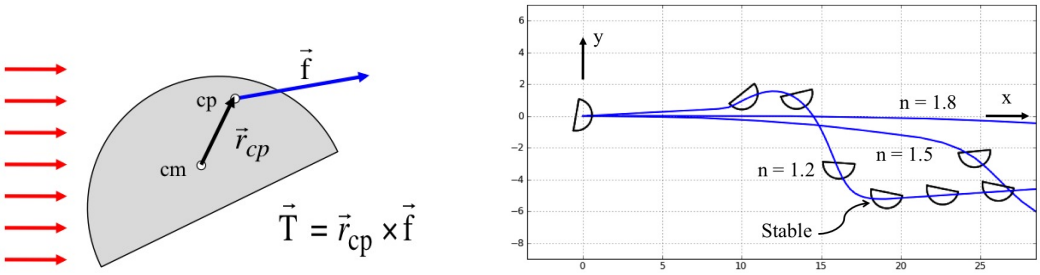

Figure 4. Left: Illustration of displaced centers of mass and pressure. At this instant in time the body rotates clockwise and accelerates upward and to the right. Right: Examples of the particle trajectory and orientation in a viscous medium for three different values of the refractive index of the wing.

If we desire torque-free forces, clearly the wing must operate at or near a position of stable rotational equilibrium. As suggested by Eq. (5), this can occur when the center of pressure vector is parallel to the force vector (i.e., the line of force intersects the center of mass), or when the displacement between the centers of mass and pressure are vanishingly small. To determine the stable rotational equilibrium positions, we must use numerical modeling, as analytical methods do not exist for this task. Examples of such modeling is described in the next section.

In a zero-damping environment such as free space, an optical wing may rotationally oscillate about an equilibrium angle: $\Delta\theta(t) = \theta(t) - \theta_{eqlm} \approx \Delta\theta_0 \cos(\omega t)$, assuming a Hooke's law restoring torque: $T \approx -k\Delta\theta$ for small values of $\Delta\theta_0$. By actively driving the oscillations in a feedback loop, one may increase or decrease the amplitude of oscillation, $\Delta\theta_0$. The frequency of oscillation is determined by the torsional stiffness, k, and the moment of inertia, I_{wing}: $\omega = \sqrt{k / I_{wing}}$. From considerations of the torque about the edge of a flat mirror, we predict this frequency to roughly scale as $\omega_0 = \sqrt{IL/cm} = \sqrt{I/c\rho A}$ where A and ρ are the cross-sectional area and mass density of the wing, respectively. For example, if I = 1 [kW/m^2], ρ = 1g/cm^3 = 10^3 kg/m^2 then $\omega_0 = \sqrt{(1/3)10^{-8}[m^2/s^2]A}$ (see plot in Fig. 5).

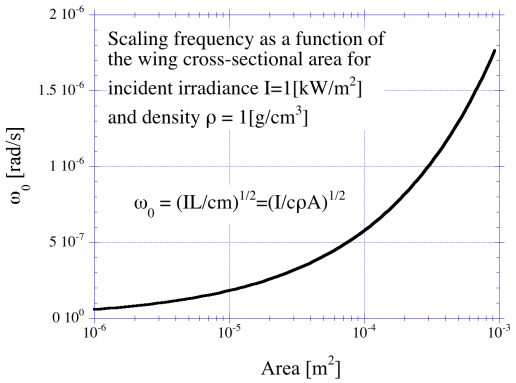

Figure 5. Frequency scaling as a function of an optical wing oscillator of cross-sectional area A.

Once the torque and force are numerically determined for all possible angles of attack, the orientation and linear positions may be determined by numerical integration (e.g., 4th order Runge-Kutta):

$$\begin{aligned} \theta(t-t_0) &= \theta_{t_0} + \dot{\theta}_{t_0} \cdot (t-t_0) + (1/2)\ddot{\theta} \cdot (t-t_0)^2 \\ x(t-t_0) &= x_{t_0} + \dot{x}_{t_0} \cdot (t-t_0) + (1/2)\ddot{x} \cdot (t-t_0)^2 \\ y(t-t_0) &= y_{t_0} + \dot{y}_{t_0} \cdot (t-t_0) + (1/2)\ddot{y} \cdot (t-t_0)^2 \end{aligned} \qquad (6)$$

where $\ddot{\theta} = T / I_{wing}$, $\ddot{x} = \mathrm{f}_x / m$, and $\ddot{y} = \mathrm{f}_y / m$. (Note that we have considered the two-dimensional case whereby other degrees of freedom are ignored.) The numerically determined phase diagram for the angle of attack, θ, and the angular velocity, $\dot{\theta}$, is shown in Fig. 6 for a semicircular wing having the flat side coated with a mirror. Note the wide range of angles (±50°) over which the wing may rock back and forth. The closed orbits in Fig. 6 may be made to spiral inward by synchronously illuminating or

shuttering the light reaching the wing. A detailed report on oscillating optical wings is included in the supplementary material, "Refractive optical wing oscillators with one reflective surface."

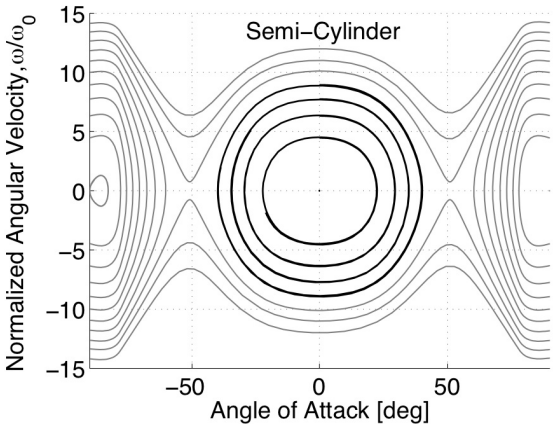

Figure 6. Phase diagram showing periodic (dark lines) rocking motion of a semicircular wing with a reflective flat side.

When any of the dimensions of the wing approaches, or becomes less than the wavelength of light, the ray-tracing model must be replaced with a wave optics model. This is necessary because interference phenomena may dominate the optical field. Further, the concept of a ray cannot be applied for cases where the optical field varies over such short distance scales. See supplementary material "Optical lift from dielectric semicylinders".

The net radiation pressure force and torque on an optical wing may be found by numerically summing over a large number of rays refracted and reflected from the surface:

$$\vec{\mathrm{f}} = \sum \vec{\mathrm{f}}_{\mathrm{i}}, \;\; \vec{T} = \vec{T}_{ex} + \vec{T}_{in} \;:\;\; \vec{T}_{ex} = \vec{r}_0 \times \vec{\mathrm{f}}, \;\; \vec{T}_{in} = \sum \vec{r}_i \times \vec{\mathrm{f}}_{\mathrm{i}} \tag{7}$$

where $\vec{T}_{ex}$ and $\vec{T}_{in}$ are respectively the extrinsic and intrinsic torque, $\vec{r}_0$ is a moment arm from the origin to the center of mass, and $\vec{r}_i$ is a vector pointing from the center of mass of the wing to the surface where a ray produces a force, $\vec{\mathrm{f}}_{\mathrm{i}}$. The intrinsic may arise when the center of mass and center of pressure are offset, e.g., when the wing is not at a position of stable rotation equilibrium. Note that intrinsic torque is zero valued for a flat rectangular reflective sail. Optical wings therefore provide a distinct new component of attitude control for solar sails. For example, an array of *N* wings (i.e., an optical flying carpet) may feel no extrinsic torque, but a multiplicative intrinsic torque. That is:

$$\vec{T}_{ex,net} = \sum_{j=1}^{N} (\vec{r}_{0,j} \times \vec{\mathrm{f}}_{\mathrm{j}}) = 0, \qquad \vec{T}_{in,net} = \sum_{\mathrm{j}=1}^{\mathrm{N}} \sum \vec{r}_{i,j} \times \vec{\mathrm{f}}_{\mathrm{i,j}} = N\vec{T}_{in} \tag{8}$$

For an array of semicircular optical wings having a reflective flat side, the intrinsic torque will provide a restoring torque. This may be particularly advantageous for a sun-facing solar sail mission such as a solar weather station at a sub-Lagrange point. By matching the rocking period of the sail to the period of the halo orbit, no fuel or mechanical parts would be needed to maintain a sun-facing orientation. Active electro-optic control methods may be used to increase or decrease angular excursions.

EXPERIMENTAL

The first experimental realization of optical lift was demonstrated with single semi-cylindrical wings. This shape was selected for early investigations of optical lift because the semicircular profile is a simplified cambered shape. Our ray-tracing computer model indicates that other wing shapes will experience optical lift and stable lift orientations when exposed to uniform illumination. The first new wing shape to be fabricated was the rectangular rod, followed by arrays of joined semi-cylindrical wings. These two objects were fabricated using photolithographic techniques. The discussed fabrication methods produced these objects with expected regularity and only minor shape artifacts. Early tests of the rectangular optical wing indicated good agreement with computer model predictions.

Following similar methodology as in the fabrication of semi-cylindrical optical wings, the new rectangular wings were made of patterned photoresist using photolithography. This process began with a 1.5μm thick layer of OiR 620 positive photoresist spin-coated onto a blank silicon wafer. OiR 620 photoresist was selected for its common use in photolithography with a refractive index of 1.6. The resist was then exposed to UV illumination with a GCA Stepper through a mask that defined the two-dimensional length and width of each wing in an array of many sizes (see background image in Fig. A). The exposed wafer was then developed to wash away excess resist, and baked on a hot plate to further solidify the resist particles. Finally, the surface of the silicon was etched in xenon hexafluoride (XeF6) for 10 hours. This released the photoresist particles, which were then collected with a surfactant-water bath.

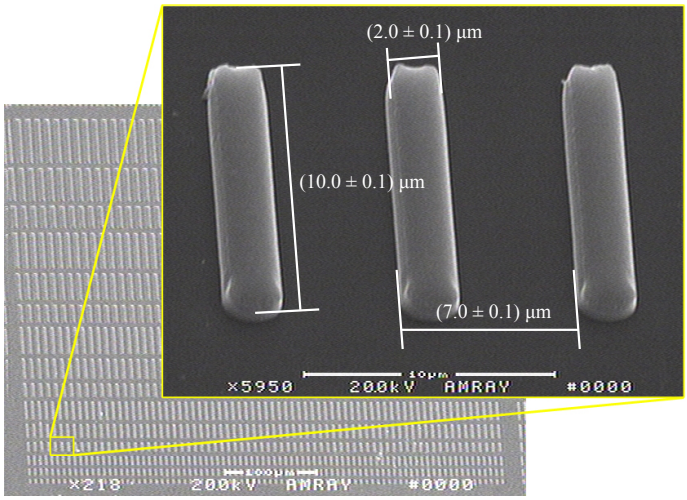

Figure A - SEM images of rectangle optical wings. Background image shows one set of wings increasing in size from the bottom of the image to the top. A sub-region is enlarged showing three 10 μm x 2 μm wings with measurements and spacing.

These fabricated rectangular were tested in a simple apparatus for determining the optical lift force incident on these objects. The submerged particles were placed in a well that was illuminated from below with a 42mW, 975nm, collimated laser beam with a diameter of 50μm. The particles were imaged through a 40x objected by a video camera such that any transverse movements of an illuminated particle were recorded. This testing indicated that the wing rotated into a stable angle of attack at roughly 50° with an approximate lift force of 3.4 pN. The same wing parameters from Fig. A were inputted into the computer model to recreate the force and torque that this particle experienced. The computer model determined that this wing rotates into a stable orientation at 54° above the horizontal as shown in Fig. B. At this stable position, the lift angle (angle corresponding to the transverse component of total force on the object) is 30°. The model predicts a lift force of 4.6pN in an ideal liquid; however, in a real fluid the force would be expected to be less than this ideal case. These computer-modeling results indicate good agreement with the tested wing.

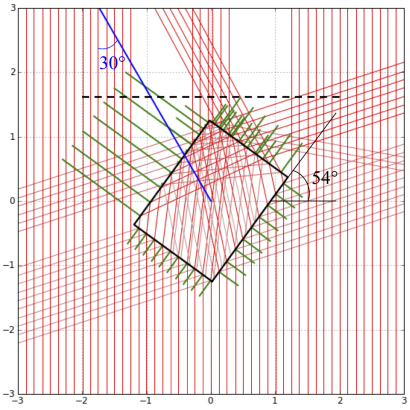

Figure B – Two-dimensional ray plot of rectangular wing from Fig. A generated by computer model. Red light rays are traveling upwards and are incident on the wing producing a total force given by the blue line. Black dashed-line is an approximation to the plane imaged by the video camera.

Several iterations have been implemented in the early fabrication stages of arrays of semi-cylindrical wings. These arrays are fabricated using isotropic reactive ion etching (RIE) to form a silicon mold. In the first trial of this fabrication technique, the mold was filled with a PDMS polymer (silicone elastomer) that was lifted from the mold by hand. This is a hydrophobic polymer with a refractive index of about 1.4. The elastomer was selected because it may be spin coated onto the silicon mold, is easily cured, and is easily managed all at low cost.

To make the silicon mold using the isotropic RIE technique a 1μm layer of thermal silicon dioxide was first grown on a silicon wafer. The oxide was then patterned with OiR 620 resist using photolithography leaving holes of exposed oxide with a range of feature sizes. Then the oxide was etched down in buffered oxide etch (BOE) for 9 minutes using the patterned resist as a mask. This exposed areas of the silicon wafer below. To achieve isotropic profiles in the silicon, the silicon was etched in the Drytek Quad with sulfur hexafluoride (SF6) using resist over oxide as an etching mask. In the first test of this process, three iterations of the Drytek etching step were implemented with different exposure times - 10, 15, and 20 minutes - all at 240 W of power, 60 mTorr of pressure, and 20 sccm of gas flow. The resist on top the oxide was cleared away in this step, and the remaining oxide was then removed again in BOE for 10 minutes leaving behind a clean silicon mold with arrays of wells. Lastly, the mold was filled with PDMS. The wafer was then degassed for 30 minutes, baked on a hot plate at 70° Celsius for 3.5 hours, and allowed to rest over night before it was peeled off the silicone substrate by hand. The process is pictorially described in Fig. C where CP1 (Colorless Polyimide 1) has taken the place of the PDMS elastomer.

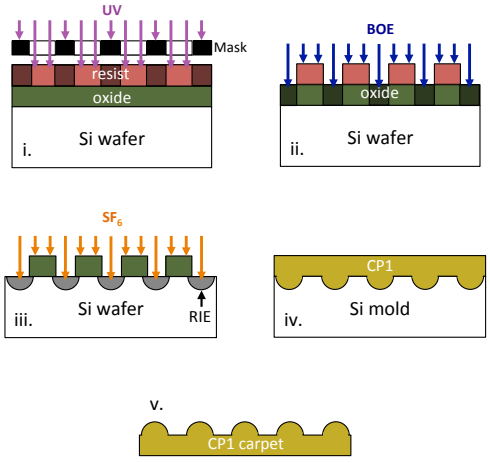

Figure C – Pictorial description of steps in fabrication of silicon mold for making semi-cylindrical wing arrays.

In the first trial with PDMS, the RIE technique did generate curved features in the silicon wafer, but the degree of curvature was small relative to the width of the features. This is due to aspect ratio dependent etching (ARDE), meaning much longer etch times would be needed to achieve semicircular profiles of this size. Smaller features are easily fabricated by the RIE process, but larger features require very long etch times that would destroy the oxide mask as occurred with the 20 minute wafer. In demolding the PDMS carpets, the polymer partially adhered to the silicon wafer, tearing the carpets, and leaving a spotty residue on the silicon.

After the first trial which produced oversized features as discussed, we successfully fabricated 180μm x 300μm x 370μm thick carpets with semi-cylindrical features that are 180μm long, 30μm wide, and 50μm tall. Fig. D below is a microscopic image of a silicon elastomer carpet. Though inexpensive and easy to work with, silicon elastomer is not a good material for fabrication of flying carpets because it is difficult to thin the substrate to less than 50μm and because the material breaks with defects as seen in Fig. D. At the first NAIC meeting, a chemist from NASA Langley informed us of the LARC-CP1 polyimide developed for solar sails. This material is more favorable for the fabrication of flying carpets because it is ultra-lightweight. It too may be spun onto the mold and released by hand.

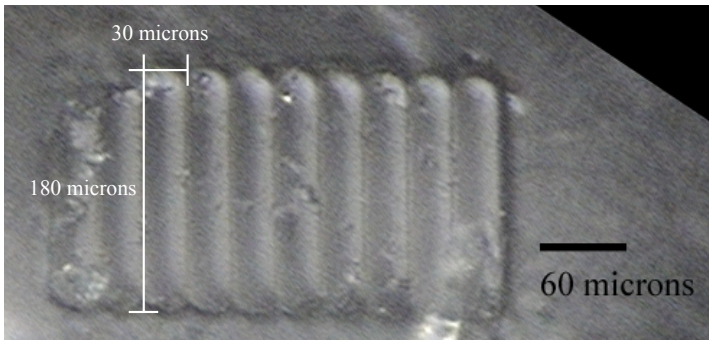

Figure D – 50x microscopic image of the smallest fabricated flying carpet mad out of silicon elastomer. Defects in the semi-cylindrical features are due to tearing of the elastomer while releasing it from the mold.

The first successful fabrication of a wing array made from CP1 was achieved near the end of the Phase I project. A 20x microscope image of these arrays on a 50 μm substrate is given in Fig. E. In addition before the end of the Phase I project, we designed a specialized mask for carpets including 1 cm^2, 1 mm^2, and 500 mm^2 linear arrays of 20 mm and 40 mm long semi-cylindrical rods with 10 and 20 μm radii.

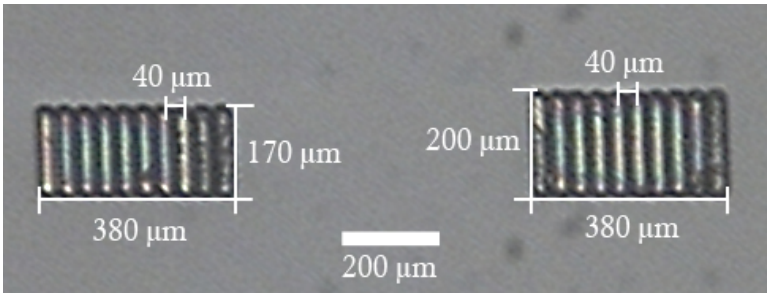

Figure E – 20x microscope image of first fabrication of CP1 arrays of semi-cylindrical wings on top a 50 mm substrate with 20 mm radii.

At the end of the Phase I project, two fabrication goals were set: 1) to decrease the substrate thickness of the CP1 arrays by improving the recipe for spin coating the resin onto the silicon mold, and 2) to fabricate single wings and arrays with mirrored back surfaces. A proposed recipe for the fabrication of these mirrored wing arrays is given in Fig. F.

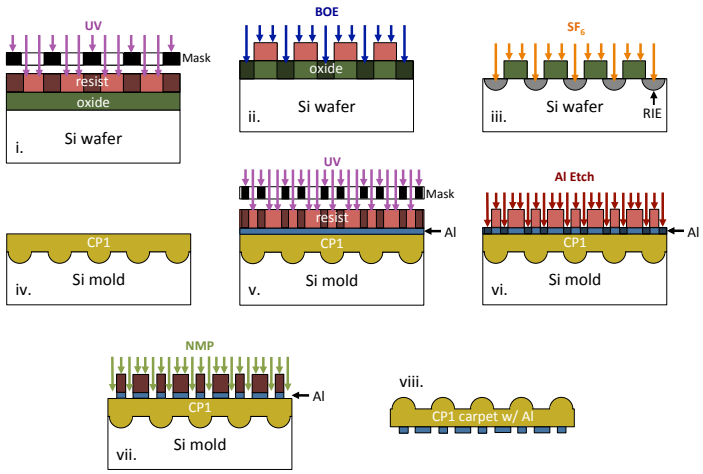

Figure F – Fabrication of mirrored wing arrays follows the same steps as were done for non-mirrored arrays with the addition of a second photoresist patterning of aluminum that would be sputtered onto the back side of CP1 substrate before releasing from the mold. Al etch would be done in a 16:1:1:2 bath of Nitric Acid, Acetic Acid, Phosphoric Acid and water, and excess resist would be removed in NMP (1-Methyl-2-pyrrolidon) solvent.

BIBLIOGRAPHY

Alhorn, D.C. and Scheierl, J.M., "FeatherSail – Design, Development and Future Impact," *NASA Technical Reports Server*, NASA, 3 May 2010. Web. 25 April 2011. <ntrs.nasa.gov/archive/nasa/casi.ntrs.nasa.gov/20100024167_2010023656.pdf>

Solar Sail Roadmap Mission GN&C Challenges, Andrew F. Heaton (NASA Marshall Space Flight Center), American Institute of Aeronautics and Astronautics

Kare, J. T., "High-acceleration Micro-scale Laser Sails for Interstellar Propulsion," *NIAC*, Universities Space Research Association, 31 December 2001. Web. 27 April 2011. <http://www.niac.usra.edu/files/studies/final_report/597Kare.pdf>

Landis, G.A., "Advanced Solar- and Laser-pushed Lightsail Concepts: Final Report," *NIAC*, Universities Space Research Association, 31 May 1999. Web. 27 April 2011. <http://www.niac.usra.edu/files/studies/final_report/4Landis.pdf>

Mulser, P. "Radiation pressure on macroscopic bodies," *J. Opt. Soc. Am. B* 2, 1814-1829 (1985).

Spieth, D., Zubrin, R, "Ultra-Thin Solar Sails for Interstellar Travel: Phase I Final Report," *NIAC,* Universities Space Research Association, December 1999. Web. 27 April 2011. <http://www.niac.usra.edu/files/studies/final_report/333Christensen.pdf>

Vulpetti, G., Johnson, L., Matloff, G.L., *Solar Sails: A Novel Approach to Interplanetary Travel*, Copernicus Books, Praxis Publishing (2008).

Vulpetti, G., "Total solar irradiance fluctation effects on sailcraft-Mars rendezvous," *Acta Astronautica* **68**, 644–650 (2011).

JAXA Press Release, "Small Solar Power Sail Demonstrator 'IKAROS' Successful Attitude Control by Liquid Crystal Device," 23 July 2010.

"NanoSail-D Latest News," www.nasa.gov/mission_pages/smallsats/nanosaild.html

Seeking a Human SpaceFlight Program Worthy of a Great Nation, NASA (2009).

Stepping-Stones to the Future of Space Exploration: A Workshop Report, National Academic Press (2004).

"Targets met for the Solar Sail IKAROS," www.scienceknowledge.org/2011/02/05/targets-met-for-the-solar-sail-ikaros

The Vision for Space Exploration, NASA (2004).

Coulter, D., and Phillips, T., "A Brief History of Solar Sails," Science @ NASA [online database], URL: http://science.nasa.gov/headlines/y2008/31jul_solarsails.htm (cited 15 December 2009).

Darling, D., "Solar Sail," The Internet Encyclopedia of Science [online database], URL: http://www.daviddarling.info/encyclopedia/S/solar_sail.html (cited 15 December 2009).

Friedman, L. D., "Projects: LightSail - The Future of Solar Sailing LightSail: A New Way and a New Chance to Fly on Light," The Planetary Society [online article], http://www.planetary.org/programs/projects/solar_sailing/tpr_lightsail.html (cited 25 March 2010).
Leary, W., "Into Orbit (Maybe Beyond) on Wings of Giant Solar Sails" New York Times, online, (21 June 2009).
Overbye, D., "Setting Sail Into Space Propelled by Sunshine," New York Times, online, (9 November. 2009).
Pappa, R., Lassiter, J., and Ross, B., Structural Dynamics Experimental Activities in Ultra- Lightweight and Inflatable Space Structures, NASA TM-2001-210857, (2001).
Scheierl, J. M. and Alhorn, D. C., Solar Sails: Design and Future Impact, NASA/MSFC/USRP Fall 2009 Intern Research Paper, Huntsville, AL (December 2009).
Stanford, N., "Hoisting the Solar Sail," Chemistry World [online database], URL: http://www.rsc.org/chemistryworld/Issues/2009/July/HoistingTheSolarSail.asp (cited 15 December 2009).
Swartzlander, G.A. Jr., Peterson, T. J., Artusio-Glimpse, A. B., and Raisanen, A. D., "Stable Optical Lift," *Nature Photonics* 5, 48-51 (2011).
Whorton, M. S, Heaton, A., Pinson, R., Laue, G., Adams, C., "NanoSail-D: The First Flight Demonstration of Solar Sails for Nanosatellites," AIAA/USU 22nd Conference on Small Satellites, SSC08-X-1, (August 2008).

Optical lift from dielectric semicylinders

Stephen H. Simpson,[1] Simon Hanna,[1] Timothy J. Peterson,[2] and Grover A. Swartzlander, Jr.[2,*]

[1]*H. H. Wills Physics Laboratory, University of Bristol, Tyndall Avenue, Bristol BS8 1TL, UK*

[2]*Chester F. Carlson Center for Imaging Science and the Department of Physics, Rochester Institute of Technology, Rochester, New York 14623, USA*

**Corresponding author: grover.swartzlander@gmail.com*

Received May 21, 2012; revised July 13, 2012; accepted July 28, 2012;
posted August 23, 2012 (Doc. ID 168768); published September 21, 2012

A wave optics numerical analysis of the force and torque on a semicylindrical optical wing is presented. Comparisons with a recently reported ray optics analysis indicate good agreement when the radius is large compared with the wavelength of light, as expected. Surprisingly, we find that the dominant rotationally stable angle of attack at $\alpha \approx -15°$ is relatively invariant to changes in radius and refractive index. However, the torsional stiffness at the equilibrium point is found to increase, approximately, as the cubic power of the radius. Quasi-resonant internal modes of light produce complex size-dependent variations of the angle and magnitude of the optical lift force.

OCIS codes: 350.4855, 350.6090, 350.6050, 350.3950.

A body in a uniform flow that experiences a force component perpendicular to the flow direction is said to experience lift. If, in addition to experiencing a lift force, the body also achieves a stable orientation, it is said to be undergoing "stable lift." In a recent article [1], an optical variant of stable lift was demonstrated for dielectric semicylinders, or *lightfoils*, exposed to plane wave illumination. Stable optical lift may be useful for propelling microscopic tissues through liquids, or for navigational and attitude control of solar sails in outer space. Here, we investigate the effect with rigorous electromagnetic calculations, ignoring viscous drag and gravity.

We consider, in two dimensions, a uniformly illuminated dielectric semicylinder of radius a and refractive index n with a host material of index $n_0 = 1$. We arbitrarily set the wavelength in the host material to $\lambda = 800$ nm, but note that the results presented are more generally applicable, owing to the scale invariance of Maxwells equations [2]; for $n_0 \neq 1$, the light foil index, n, must be replaced by n/n_0, the quoted radii by a/n_0, and the forces and torques by $n_0 f$, $n_0 t$, respectively [3].

A schematic showing the axes and angles used is provided in Fig. 1. The lift force is given by the component $f_y = |f| \sin \phi_f$, whereas the scattering force may be written $f_x = |f| \cos \phi_f$, where ϕ_f is the lift angle. The orientation of the lightfoil is represented by the angle of attack, α; the origin of coordinates is coincident with the center of mass. The forces and torques quoted are given as ratios of the lightfoil length, L (μm), in the z direction, for an incident wave carrying $I = 1$ mW/μm^2. In these units, a light foil experiencing a force of 1 pN per μm radius, per μm length has an optical force efficiency, $Q = cf/I$, of $c/10^9 \approx 0.30$ or 30% compared with an ideal mirror of efficiency 2 or 200%.

Optical scattering from semicylinders has previously been studied analytically, under restricted conditions [4]. Here, we apply the generalized multipole method [5,6] with cylindrical vector wave functions [7]. Forces and torques are evaluated by integrating the Maxwell stress tensor over a surface enclosing the lightfoil [3,8]. Stable orientations (α_{eqm}) are found by considering the variation of axial torque (t_z) with lightfoil orientation (α), locating the angles at which t_z vanishes and confirming that t_z is locally restoring. We note that, in general, the stability of a rigid body depends on coupling between translational and rotational motion [9]. However, under plane wave illumination, and in vacuo, translations cannot produce rotations and the condition that the torque is restoring is both necessary and sufficient for stability in two dimensions. Since elongated dielectric objects seek to align themselves with the electric polarization direction [10], attention is restricted to the transverse electric case, with the electric field polarized in the z direction.

Figure 2 shows the ratios $f_{x,y}/La$ and t_z/La^2 as functions of α, for lightfoils with $n = 1.3$, and various radii, a. For scaling purposes, the length of the cylinder is taken to be $L = 1$ μm. Three effects are evident. First, for larger radii, the curves tend to converge, indicating that the forces increase in proportion to La, and the torque increases as La^2. Second, when the light is incident on the flat surface of the lightfoil ($0 < \alpha < 180°$), forces and torques become increasingly oscillatory as the radius is increased. Finally, several equilibrium orientations are evident in each case. When $\alpha = \pm 90°$, there is no lift force, owing to symmetry, and what is more, the lightfoil is in an unstable rotational equilibrium state (i.e., $dt_z/d\alpha > 0$). In contrast, a strong restoring torque with $dt_z/d\alpha < 0$ produces a stable rotational equilibrium at $\alpha \approx -15°$. Ray optics calculations [1] are also shown in the figure. In this case, size effects are neglected and the oscillations in the forces and torques that arise due to interference and diffraction do not appear.

In order to quantify these observations, it is necessary to isolate the equilibria of interest and evaluate the excess force in the stable orientation. Results for lightfoils

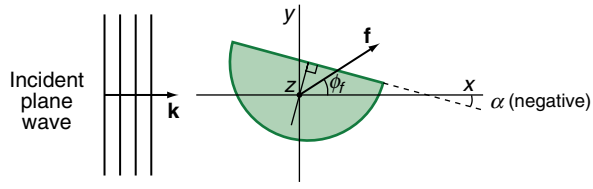

Fig. 1. (Color online) Schematic showing the axes and angles used in the text. The angle of attack, α, and the angle at which the excess force acts, ϕ_f, are measured counterclockwise from the positive x-axis.

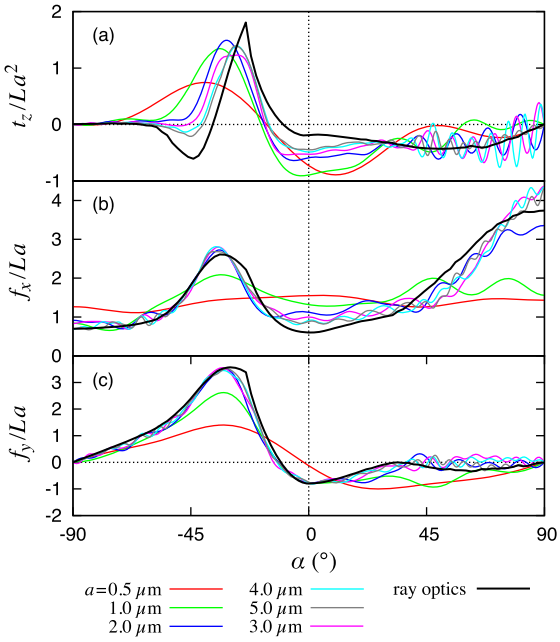

Fig. 2. (Color online) Forces and torques experienced by lightfoils with $n = 1.3$, $L = 1$ μm, and various radii, a. (a) Scaled axial torque, t_z/La^2 (pN/μm^2), (b) scattering force, f_x/La, and (c) lift force, f_y/La (pN/μm^2).

with six different refractive indices, and radii varying in the range from 0.1 to 5 μm are shown in Fig. 3. For radii less than about one quarter of a wavelength, α_{eqm} changes very rapidly, falling from about 20° to −15°. Thereafter, the behavior is strongly dependent on n. For low indices (corresponding to, say, silica glass in water), α_{eqm} remains fairly steady as a is increased. However, for

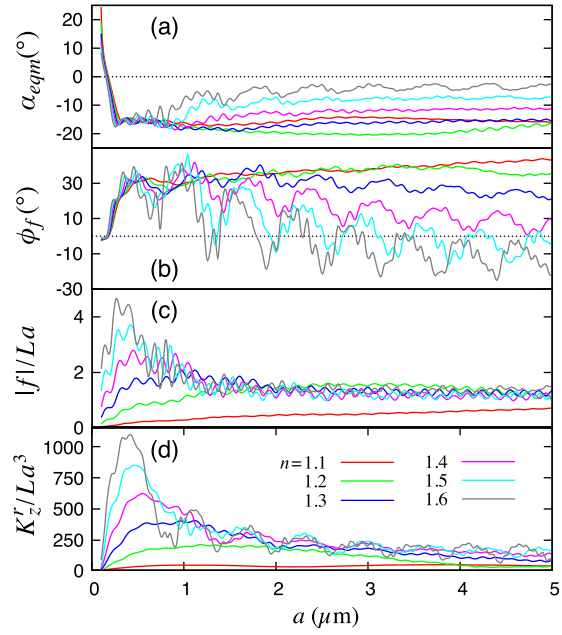

Fig. 3. (Color online) Stable equilibrium conditions for lightfoils of length 1 μm, with six distinct refractive indices, and $0.1 < a < 5$ μm. (a) Angle of attack, α_{eqm}, (b) lift angle ϕ_f, (c) scaled force modulus, $|f|/La$ (pN/μm^2), and (d) scaled torsional stiffness, K_z^r/La^3 (pN/deg.μm^3).

higher n (e.g., silica in air), α_{eqm} declines with increasing radius until the flat surface of the light foil is almost parallel to the direction of propagation.

The lift angle, ϕ_f, shows a more pronounced effect [Fig. 3(b)]. Once more, the variation is relatively independent of n in the low radius regime and the subsequent changes in angle for low index semicylinders are relatively minor. However, for higher index materials, the lift angle oscillates dramatically. These oscillations occur with two distinct periods and derive from geometric resonances of the structure. The more rapid oscillations correspond to half integer wavelengths across the diameter of the lightfoil; i.e., they resemble the oscillations in the reflectivity of a dielectric lamina with increasing thickness. The slower oscillation is more difficult to understand: it appears to relate to integer numbers of wavelengths over the radius (in that these coarser oscillations have a period of about four times that of the finer ones).

Figure 3(c) shows the modulus of the force acting at mechanical equilibrium as a ratio of the radius a. Apart from the rapid oscillations mentioned above, these curves, once more, approximately converge for larger refractive indices. Finally, Fig. 3(d) shows the torsional stiffness, $K_z^r = -dt_z/d\theta_z$, as a ratio of the cube of the radius. It is more difficult to ascribe an appropriate power law to this quantity. K_z^r initially increases much faster than a^3 before appearing to flatten out at larger radii. Despite the complex resonant behavior for higher refractive index lightfoils, favorable sets of parameters exist. For example, when the radius is exactly one or two wavelengths in the material, lift angles are high as are the force magnitudes.

In order to provide a clearer understanding of the parameter space, similar equilibrium searches are performed for a range of refractive indices and radii. Figure 4(a) shows the variation in α_{eqm}. As observed above, α_{eqm} varies rapidly for narrow cylinders of all refractive indices. For larger radii, it is relatively steady and, across much of the parameter space, it has a value of $\alpha_{\mathrm{eqm}} \approx -15°$. The lift angle ϕ_f [Fig. 4(b)] is more susceptible to size effects. For lower refractive indices, which could correspond, for example, to polystyrene in water, lift angles do not oscillate too wildly with size and $\phi_f \approx 35$–$40°$. For higher refractive indices, ϕ_f is more erratic. Although obviously propitious sets of parameters are evident, care must be taken to avoid structures with low or negligible lift. For this reason, design of optimal wavelength-scale lightfoils requires control of dimensions to tolerances of fractions of a wavelength. The modulus of the force at equilibrium is shown in Fig. 4(c) as a ratio to the radius. As with each of the other quantities discussed, it shows oscillatory behavior, associated with geometric resonances, but is otherwise invariant over much of the parameter space. Finally, the scaled torsional stiffness, K_z^r/La^3, is shown in Fig. 4(d), confirming the approximate scaling law, $K_z^r \propto a^3L$, for lightfoils with radii larger than about two wavelengths. The moment of inertia of the lightfoil, about its long axis, increases as a^4L. Hence, in a vacuum, an angular perturbation from equilibrium will result in oscillations of frequency $\propto 1/\sqrt{a}$. Conversely, in a viscous fluid, the hydrodynamic resistance varies as $\sim a^2L$

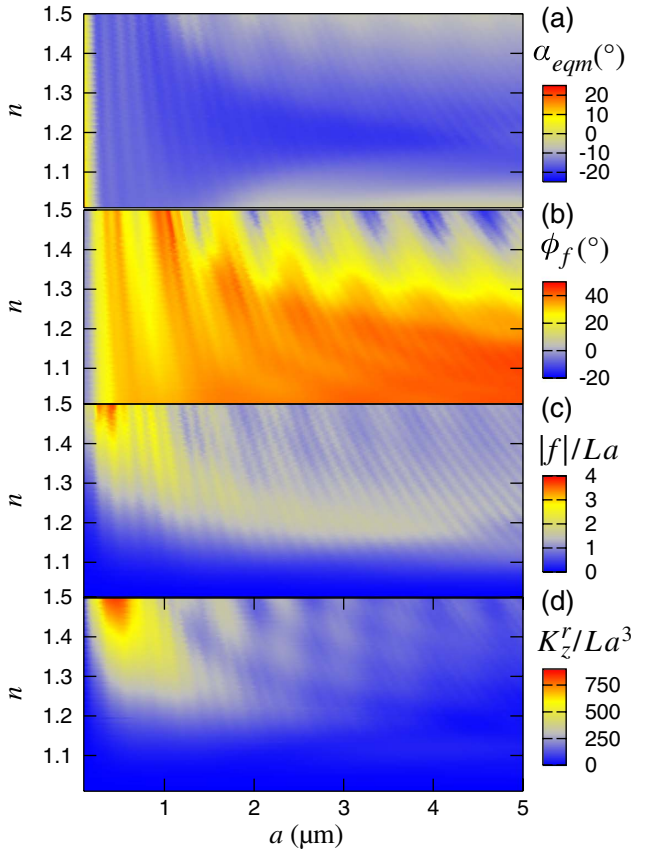

Fig. 4. (Color online) (a) Angle of attack at equilibrium, α_{eqm}, (b) lift angle, ϕ_f, (c) scaled force modulus, $|f|/La$ (pN/μm^2), and (d) scaled torsional stiffness, K_z^r/La^3 (pN/deg.μm^3), as functions of n and a.

[11], and the lightfoil relaxes back to equilibrium with a time constant that is proportional to a. These remarks are purely qualitative; a more rigorous treatment of the stability and motion of lightfoils will form the basis of a future publication.

To illustrate that these structures are indeed capable of flight, we consider two examples. The first is a lightfoil with a radius of 3.75 μm and length 100 μm, made from a material with a refractive index of 1.6 and a density of 1.5 gcm^{-3}, immersed in water (refractive index 1.333). Its weight in water is then ≈20 pN. The size of the optical lift force that it experiences is that of a $1.33 \times 3.75 = 5.0$ μm radius rod of refractive index $1.6/1.333 = 1.2$ in vacuum, multiplied by 1.333; i.e., the lift force is ≈240 pN in a 1 mW/μm^2 plane wave. A plane wave with power ≈0.1 mW/μm^2 is required to lift this light foil in water. A similar calculation for a silica lightfoil with radius 1 μm in air indicates that in this case about 0.4 mW/μm^2 is required.

In this Letter, we have shown that dielectric semicylinders exposed to plane wave illumination have a stable equilibrium orientation that is approximately independent of size and refractive index. The stability arises partly because of the lightfoil geometry, and partly because translational motion under plane wave illumination cannot induce a torque. The net lift force arises due to asymmetric deviation of the momentum of the incident light as it passes through the lightfoil. We predict the lift force experienced in the present configuration is great enough to overcome gravity for irradiance values ~10 kW/cm^2, in agreement with experiments [1]. Finally, the lift force and stable orientation are subject to geometric resonances for larger values of refractive index, which correlate with the incident wavelength.

We are grateful to Alexandra Artusio-Glimpse, Rochester Institute of Technology, for discussions on experimental aspects of optical lift. G. Swartzlander acknowledges support from the NASA Innovative Advanced Concepts Office (NIAC), Grant No. NNX11AR40G.

References

1. G. A. Swartzlander, Jr., T. J. Peterson, A. B. Artusio-Glimpse, and A. D. Raisanen, Nat. Photonics **5**, 48 (2011).
2. M. Mishchenko, J. Quant. Spectrosc. Radiat. Transfer **101**, 404 (2006).
3. R. N. C. Pfeifer, T. A. Nieminen, N. R. Heckenberg, and H. Rubinsztein-Dunlop, J. Opt. **13**, 044017 (2011).
4. A. Gautesen, R. Ziolkowski, and R. McLeod, SIAM J. Appl. Math. **51**, 1556 (1991).
5. C. Hafner, *The Generalized Multipole Technique For Computational Electrodynamics* (Artech House, 1990).
6. F. Kahnert, J. Quant. Spectrosc. Radiat. Transfer **79**, 775 (2003).
7. C. F. Bohren and D. R. Huffman, *Absorption and Scattering of Light by Small Particles* (Wiley-VCH, 1983).
8. J. A. Stratton, *Electromagnetic Theory* (Adams, 2007).
9. S. H. Simpson and S. Hanna, Phys. Rev. E **82**, 031141 (2010).
10. S. H. Simpson, D. C. Benito, and S. Hanna, Phys. Rev. A **76**, 043408 (2007).
11. S. Kim and S. J. Karrila, *Microhydrodynamics: Principles and Selected Applications* (Dover, 2005).

Refractive optical wing oscillators with one reflective surface

Alexandra B. Artusio-Glimpse,* Timothy J. Peterson, and Grover A. Swartzlander, Jr.

Chester F. Carlson Center for Imaging Science, Rochester Institute of Technology,
54 Lomb Memorial Dr., Rochester, NY 14623, USA
* *Corresponding author: aba5677@rit.edu*

Compiled January 8, 2013

An optical wing is a cambered rod that experiences a force and torque owing to the reflection and transmission of light from the surface. Here we address how such a wing may be designed to maintain an efficient thrust from radiation pressure while also providing a torque that returns the wing to a source facing orientation. The torsional stiffness of two different wing cross-sections is determined from numerical ray-tracing analyses. These results demonstrate the potential to construct a passive sun-tracking, space flight system or a micro-scale surface measurement device based on radiation pressure and torque.

OCIS codes: 350.4855, 350.6090, 350.3950.

The ability of light to push an object, first described by Maxwell, is simple to describe in closed form for a flat reflecting or absorbing surface. An arbitrarily shaped object, however, often requires computer modeling to determine the forces and torques created by radiation pressure. Optical torque may arise owing to an offset of the center of mass and center of radiation pressure (RP). Many research opportunities and potential applications are afforded by considering different shapes and optical properties of the body, as well as different irradiance distributions. The effects of RP are particularly significant in low gravity environments such as outer space or neutrally buoyant liquids.

The remarkable history of early uses of radiation pressure in outer space includes the 1974 rescue of the Mariner 10 mission to Venus and Mercury. Various international space agencies are currently testing and pursuing the development of solar sailcrafts [1]. New modalities to control the force and torque on sailcrafts are being sought for attitude and navigation purposes [2]. Current means to affect the sailcraft attitude, and thus the thrust vector, include the use of ballast masses [3], tip vanes [4,5], and actively controlled liquid crystal scatterers [6]. Bench-top RP experiments powered by focused laser beams, rather than uniform sunlight, proliferated after Ashkin's development of optical tweezers [7]. Control over additional degrees of freedom was afforded by use of spatial light modulators [8]. Bessel beams have recently been shown to provide opportunities to either attract or repel a particle from the source of light [9–11]. Molding the shape of the particle, rather than the light field, has opened other recent avenues of exploration. Examples of this approach include optically driven micro-gears and rotors [12–14], and optical wings [15, 16].

This Letter describes an enabling radiation pressure component that accomplishes a fundamental task that has no analog for a flat reflecting surface. We predict that an optical wing having a reflective coating over part of the surface will experience a restoring torque that returns the element to a sun facing (or light-source facing) orientation. Single elements may be used as microscopic mechanical oscillators, and arrays may be used for attitude control of a sailcraft. For example, we envision the placement of such arrays on a station keeping sailcraft to achieve a passive sun-facing attitude control within the halo orbit of a sub-Lagrange point [17]. In addition to sails, the tunable rotation periods of the presented optical wings may be useful to the microbiology field for surface tension measurements, material transport, and other applications.

Optical wings are cambered objects that experience both a lift force and a torque due to reflection and refraction of quasi uniform illumination at the wing surface. The lift force and torque on purely refractive cambered objects have previously been discussed in [15, 16]. We have since discovered that inclusion of a mirrored back surface gives the wings special properties, namely a restoring torque that fixes the wing to oscillate about normal incidence with the refractive side facing the source. Two optical wing oscillator designs are analyzed below: the semi-cylinder and the trapezoidal rod both of length L >> 2R,B, Fig. 1.

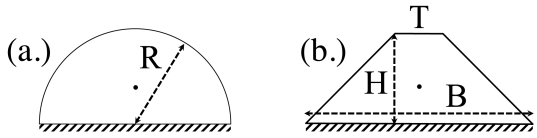

Fig. 1: Diagram of two wing oscillators with equal mass having reflective back surfaces. (a) Semi-cylinder: R = 0.5 units. (b) Trapezoidal rod: T = 0.21, H = 0.30, and B = 1.0 units.

The optical lift force is transverse to both the direction of propagating light and the scatter force. This force arises from the shape and orientation of the optical wing, which differs from the gradient force that arises from highly focused Gaussian beams [7]. The total force on a wing consists of both lift and scatter components, and may be described as originating at the center of optical pressure (CP). The force on an object from light of inten-

sity I is given by $F = QIA_s/c$, where A_s is the source-facing area equal to 2RL or BL for the semi-cylinder or trapezoidal rod, respectively, c is the speed of light, and Q is the effective fraction of light reflected. A perfect mirror at normal incidence has a value $Q = 2$. This value changes as a function of angle of attack, α. The total force may be described in terms of lifting and scattering such that $Q = \sqrt{Q_x^2 + Q_z^2}$, where Q_x and Q_z are the lifting and scattering components with maximum values of 1 and 2, respectively.

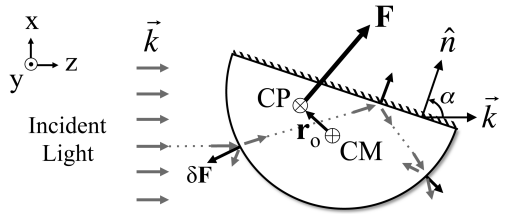

Fig. 2: Free body diagram of semi-cylindrical wing of infinite length, where $\mathbf{r}$ is the vector offset from the center of mass (CM) to the center of pressure (CP) such that the torque due to total force $\mathbf{F}$ is $\mathbf{T} = \mathbf{r}_0 \times \mathbf{F}$.

Optical torque about an object center of mass (CM) due to a small force $d\mathbf{F}$ on a surface element is given by $d\mathbf{T} = \mathbf{r} \times d\mathbf{F}$, where $\mathbf{r}$ is a vector from the center of mass to the surface point. The net torque may be expressed $\mathbf{T} = \oint(\mathbf{r} \times d\mathbf{F}) = \mathbf{r}_0 \times \mathbf{F}$ where $\mathbf{F}$ is the net force and $\mathbf{r}_0$ defines the CP-CM offset, Fig. 2. A Q-factor may be defined for the optical torque $\mathrm{T} = \mathrm{R}(IA_s/c)Q_t$, where $Q_t = Q(r_0/\mathrm{R})$ and R is one-half the object sun-facing width, i.e., equal to R or B/2 for the respective objects in Fig. 1. The values of $Q(\alpha)$, ie. force and torque efficiencies, must be determined numerically.

In our ray-tracing model, a large number of rays are refracted and reflected by an input object until the intensity of the internal rays become negligible. The momentum transfer from each ray is summed to obtain the total force on the wing. We find that both wing designs in question have zero lift force and torque at normal incidence ($\alpha = 0°$), yet stably oscillate when initially positioned at an angle of attack. We also find that $Q_z(\alpha = 0) \approx 2$ for the trapezoidal wing (~ 0.25 for the semi-cylinder).

To visualize the free flight trajectories of these optical wings, phase diagrams in Fig. 3 plot the angular velocity of each wing as a function of angle of attack for n = 1.5. Each contour line is a path of constant energy in the (α, ω) plane. The contours are separated by $10[J\omega_0^2]$ unit-less energy units, where J is the moment of inertia of the wing and $\omega_0 = \sqrt{I\mathrm{L}/cm}$, where m is the mass of the wing. From the phase diagram, we notice that near $\alpha = 0°$ there are stable orbits highlighted in black. With too much initial angular velocity, the wings go into a tumble. Rotated to too great an angle of attack, the wings no longer follow a stable orbit about $\alpha = 0°$.

To either side of normal incidence, the wing may be oriented into a rotationally unstable angle of attack.

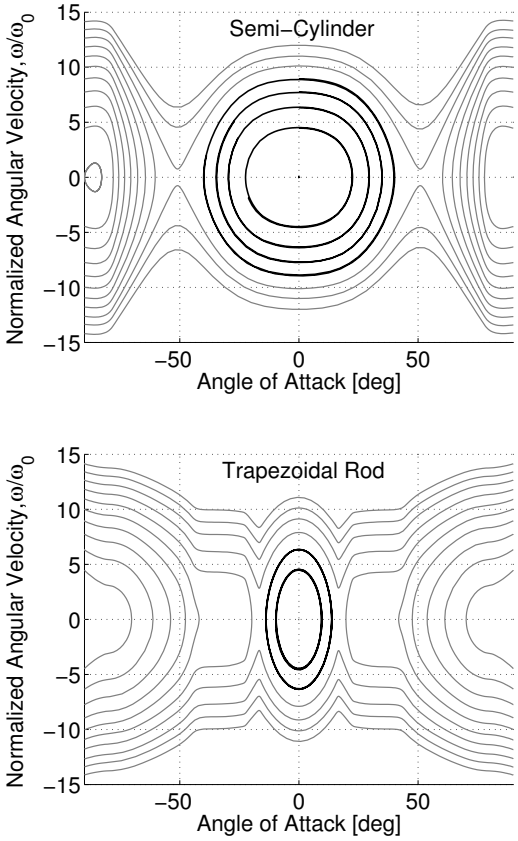

Fig. 3: Phase diagram at n = 1.5 for (a) semi-cylinder and (b) trapezoidal rod. Contours separated by $10[J\omega_0^2]$.

These angles define the maximum rotation that can be applied to the wing for oscillation to occur. At a relative refractive index of 1.5, the trapezoidal rod has a much narrower stable region from $\pm 17°$ than does the semi-cylinder, ranging from $\pm 51°$. As an approximation, we can portray these optical wings as simple harmonic oscillators within the stable regions to obtain a rotational stiffness k_α, where $\mathrm{T} \approx -k_\alpha \alpha$.

The oscillation period due to optical torque on a wing is related to the rotational stiffness by $P = 2\pi\sqrt{J/k_\alpha}$, where k_α scales with the power of light across the wing (IA_s) and R. A semi-cylindrical wing made of OIR 620 photoresist (n = 1.6, R = 0.8 μm, L = 10 μm, and $m = 12$ pg) oscillates with a damp-free period of 1.2 ms when exposed to 10 $\mu W/\mu m^2$ of light. If this same semi-cylinder were placed in earth gravity ($g = 9.8$ m/s) on a flat surface curved-side down, it would rock with a damp-free period of approximately 3.4 ms due to an offset of the wing center of mass to the position of the normal force when the wing is rotated by a small angle. This gravitational period of oscillation of the semi-cylinder is given by $P = 3\pi\sqrt{\mathrm{R}\pi/2g}$.

Let us now explore rotational stiffness as a function of refractive index, n, of the two wings. This is important for broadband illumination (e.g. solar). The values for rotational stiffness are given relative to the stiff-

ness of a mirror rotating about one edge such that $Q_t = -2|\sin(\alpha)|\sin(\alpha) \approx -0.2\alpha$, for small α.

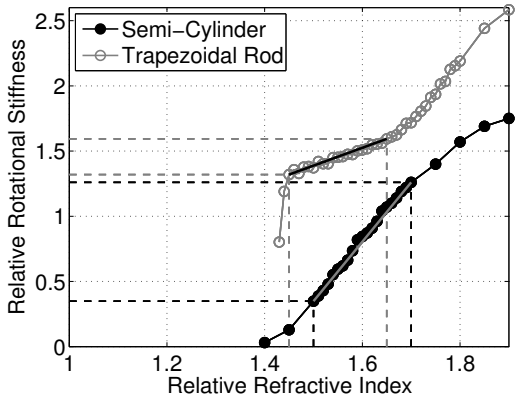

Fig. 4: Relative rotational stiffness against refractive index. Trapezoid curve is straight between 1.45 and 1.65, and semi-cylinder curve is straight between 1.5 and 1.7.

Both wing shapes increase in stiffness with refractive index, as shown in Fig. 4. They also both have a straight-line portion in the curve where the growth is linear. The trapezoidal rod is stiffer than the semi-cylinder for all indexes of refraction. In applications using broadband illumination, small change in stiffness with refractive index may be desirable. With a straight-line slope of only 0.77 as apposed to 2.55, the stiffness of the trapezoid changes more slowly than does the semi-cylinder. There is also a cut-off refractive index below which the wings become rotationally unstable. The cut-off index for the semi-cylinder is 1.37 and for the trapezoid is 1.41. These unstable indexes are undesirable for oscillators.

There may be applications of optical wing oscillators making use of the curved surface of the semi-cylinder. For example, a semi-cylinder placed curved side down on a microscope slide would rock from side to side on the slide when exposed to light. Any losses to the period of the rocking would be an indication of the surface tension between the wing and the slide.

To scale-up optical torque, many wings may be joined together to form a wing array with a total torque $\mathrm{T}_t = N\mathrm{T}$, where N is the number of wings in the array. Additional torques that arise from the shifting of wings from the pivot point of a larger object like a solar sail may be avoided by insuring a balance of wings to either side of the pivot point. As such, only the optical torque from the wings T_t would be applied to the large craft. For example, given two arrays of 1000 millimeter-scale, semi-cylindrical wings placed equidistant from the center of a 67x67m solar sail made of CP1 [18], the sail would passively follow an orbit with a period of 3 years when uniformly exposed to 1500 $\mathrm{W/m^2}$ intensity of light.

Through the example of two optical wing designs, we have numerically shown that optical wing oscillators are orbitally stable. The trapezoidal rod presented meets many beneficial design parameters such as high scattering force for forward thrust, large rotational stiffness, low change in stiffness with respect to refractive index, and rotational stability near normal incidence for a range of glass refractive indexes. However, the trapezoidal rod has a small angular region where stable oscillation is possible. On the other hand, the semi-cylinder is stable over a large range of angles and its curved surface provides other opportunities for rotation-based applications. Optical wing oscillators with large rotational stiffness are expected to be robust to perturbations and may be used to passively maintain periodic orbits of solar sails or used in micro-scale investigations.

This work was supported by NASA under award No. NNX11AR40G. A. Artusio-Glimpse a NSF Graduate Research Fellow. We are grateful to Charles L. Johnson, NASA Marshall Space Flight Center, and Alan D. Raisanen, Rochester Institute of Technology, for instructive discussions.

References

1. R. Kezerashvili, ed., *Proceedings of the Second International Symposium on Solar Sailing* (New York City College of Technology, 2010).
2. C. R. McInnes, *Solar Sailing: Technology, Dynamics and Mission Applications* (Springer, 2004).
3. D. Romagnoli and T. Oehlschlagel, Advances in Space Research **48**, 1869 (2011).
4. B. Wie, Journal of Guidance, Control, and Dynamics **27** (2004).
5. E. Mettler, A. B. Acikmese, and S. R. Ploen, "Attitude dynamics and control of solar sails with articulated vanes", Tech. rep., Guidance and Control Analysis Group, Jet Propulsion Laboratory (2005).
6. Y. Tsuda, O. Mori, R. Funase, H. Sawada, T. Yamamoto, T. Saiki, T. Endo, K. Yonekura, H. Hoshino, and J. Kawaguchi, Acta Astronautica (2012).
7. A. Ashkin, Physical Review Letters **24**, 156 (1970).
8. D. Grier, Nature Photonics **424**, 810 (2003).
9. J. Chen, J. Ng, Z. Lin, and C. T. Chan, Nature Photonics **5**, 531 (2011).
10. J. J. Sáenz, Nature Photonics **5** (2011).
11. D. Ruffner and D. Grier, Physical Review Letters **108** (2012).
12. N. K. Metzger, M. Mazilu, L. Kelemen, P. Ormos, and K. Dolakia, Journal of Optics **13** (2011).
13. P. Galajda and P. Ormos, Applied Physics Letters **80**, 4653 (2002).
14. T. Asavei, V. L. Y. Loke, M. Barbieri, T. A. Nieminen, N. R. Heckenberg, and H. Rubinsztein-Dunlop, New Journal of Physics **11** (2009).
15. G. A. Swartzlander, T. J. Peterson, A. B. Artusio-Glimpse, and A. D. Raisanen, Nature Photonics **5**, 48 (2011).
16. S. H. Simpson, S. Hanna, T. J. Peterson, and G. A. Swartzlander, Optics Letters **37**, 4038 (2012).
17. J. Bookless and C. R. McInnes, Acta Astronautica **62**, 159 (2008).
18. R. Osiander, M. A. G. Darrin, and J. L. Champion, eds., *MEMS and Microstructures in aerospace applications* (CRC Press, 2005).